

Efficient Fluid-Structure Interaction Simulation of Viscoplastic and Fracturing Thin-Shells Subjected to Underwater Shock Loading

Ralf Deiterding, Fehmi Cirak, and Sean P. Mauch

The fluid-structure interaction simulation of shock-loaded thin-walled structures requires numerical methods that can cope with large deformations as well as local topology changes. We present a robust level-set-based approach that integrates a Lagrangian thin-shell finite element solver with fracture and fragmentation capabilities into an Eulerian Cartesian fluid solver with embedded boundary and mesh adaptation capability. As main computational applications, we consider the plastic deformation and rupture of thin plates subjected to explosion and piston-induced pressure waves in water.

1 Introduction

The construction of efficient and scalable algorithms for simulating shock-driven fluid-structure interaction (FSI) problems is an area of active research. The discretizations both in fluid and solid are usually time-explicit and therefore computationally comparably inexpensive. On the other hand, major geometric complexities, such as large structural deformations, fracture, and even fragmentation might have to be considered. An approach to this problem is to employ an immersed or embedded boundary method in the fluid solver (Mittal and Iaccarino, 2005), in which moving solid structures slide through a fixed (Eulerian) fluid background mesh.

We have developed a generic software framework for shock-driven FSI simulation, named *Virtual Test Facility* (Deiterding et al., 2006b), that imposes embedded moving wall boundary conditions on a Cartesian fluid solver with a ghost fluid approach, as proposed by Fedkiw (2002) and Arienti et al. (2003). A scalar level set function storing the distance to the nearest element of the solid's triangulation is utilized to represent the embedded geometry on the fluid grid and block-based dynamic mesh adaptation is employed to mitigate boundary approximation inaccuracies. The Virtual Test Facility (VTF) specifically targets coupled problems in the high-speed regime, such as the transient deformation of metallic structures due to explosive detonations or the fracture and fragmentation of brittle or ductile materials under shock wave impact, cf. Aivazis et al. (2000) and Mauch et al. (2003). Computational fluid and solid mechanics solvers are time-accurate and consider all arising supersonic wave phenomena (e.g., shear and dilatation waves in the viscoplastic solid, shock waves in the compressible fluid) correctly. For coupling, a temporal splitting technique, in which solvers exchange data only at the interface between disjoint computational domains after consecutive time steps, is adopted. For compressible fluids, stable solutions are obtained reliably with such a *weakly coupled* method, when the evolving interface geometry and velocities are imposed as boundary conditions on the fluid solver and the hydrodynamic pressure is used as force boundary condition acting on the solid exterior, cf. Löhner et al. (2003), Cirak and Radovitzky (2005), and Specht (2000).

While the VTF approach has been successfully applied to verification and validation examples driven by shock and detonation waves in gases, cf. Deiterding et al. (2006a) and Deiterding et al. (2006c), we focus here primarily on thin-walled solid structures subjected to strong pressure waves in water. In Section 2, we sketch the adaptive Cartesian finite volume fluid solver with level-set-based embedded boundary capability and briefly describe the employed multiphase Riemann solver. Section 3 outlines the solid mechanics solver that has been developed to enable FSI simulations of thin-walled (possibly fracturing) shell structures. In Section 4, we outline the highly efficient auxiliary algorithm based on geometric characteristic reconstruction and scan conversion that we have developed to transform evolving triangulated surface meshes efficiently into signed or unsigned distance functions. The fluid-structure coupling algorithm, highlighting its incorporation into the adaptive fluid mesh refinement framework is detailed in Section 5. The simple verification test of an elastic beam under shock loading is

discussed in Section 6.1. Sections 6.2 and 6.3 present FSI simulation results for two setups involving viscoplastic deformation and fracture of thin circular isotropic metal plates subjected to shock loadings from or comparable to underwater explosions. Good agreement with experimental results and the level of detail provided make the computations excellent test cases for explicit FSI software.

2 Eulerian fluid mechanics solver

In this section, we are concerned with the construction of an Eulerian fluid solver suitable for efficient fluid-structure coupling. Although the presentation is tailored to the two-component solver employed throughout this paper, the concepts are equally applicable to other conservation laws with or without source terms, cf. Deiterding et al. (2006c).

2.1 Governing equations

The simulation of trans- or supersonic wave phenomena in fluids requires the consideration of the compressibility while viscosity can typically be neglected. The basic system of governing equations are the Euler equations:

$$\partial_t \rho + \nabla \cdot (\rho \mathbf{u}) = 0, \quad \partial_t (\rho \mathbf{u}) + \nabla \cdot (\rho \mathbf{u} \otimes \mathbf{u}) + \nabla p = 0, \quad \partial_t (\rho E) + \nabla \cdot ((\rho E + p) \mathbf{u}) = 0. \quad (1)$$

Herein, ρ is the density, \mathbf{u} the velocity vector and E the specific total energy. In order to close (1), an equation of state $p = p(\rho, e)$ is required for modeling the dependency of the hydrostatic pressure p on density ρ and specific internal energy $e := E - \frac{1}{2} \mathbf{u}^T \mathbf{u}$. For a single polytropic gas, the equation of state (EOS) reads

$$p = (\gamma - 1) \rho e \quad (2)$$

with γ denoting the constant adiabatic exponent. For Eq. (2), the speed of sound in the fluid c is found to be $c = (\gamma p / \rho)^{1/2}$. For very high pressures, as they appear for instance in underwater explosions, a simple extension of Eq. (2) to the *stiffened* gas EOS of the form

$$p = (\gamma - 1) \rho e - \gamma p_\infty \quad (3)$$

is sufficient to model pressure waves in liquids with speed of sound $c = (\gamma (p + p_\infty) / \rho)^{1/2}$. Equation (3) becomes the EOS of a multi-component mixture if we assume a model based on the volume fractions α^i , with $\sum_{i=1}^m \alpha^i = 1$, that defines the mixture quantities as

$$\rho = \sum_{i=1}^m \alpha^i \rho^i, \quad \rho \mathbf{u} = \sum_{i=1}^m \alpha^i \rho^i \mathbf{u}^i, \quad \rho e = \sum_{i=1}^m \alpha^i \rho^i e^i, \quad \frac{p}{\gamma - 1} = \sum_{i=1}^m \frac{\alpha^i p^i}{\gamma^i - 1}, \quad \frac{\gamma p_\infty}{\gamma - 1} = \sum_{i=1}^m \frac{\alpha^i \gamma^i p_\infty^i}{\gamma^i - 1},$$

and in which each component satisfies a stiffened gas EOS of the form $p^i = (\gamma^i - 1) \rho^i e^i - \gamma^i p_\infty^i$. At this point, several possibilities would exist to derive different sets of governing transport equations for a two-fluid model, however, we choose to follow the approach of Shyue (1998) that supplements system (1) with the two advection equations

$$\frac{\partial}{\partial t} \left(\frac{1}{\gamma - 1} \right) + \mathbf{u} \cdot \nabla \left(\frac{1}{\gamma - 1} \right) = 0, \quad \frac{\partial}{\partial t} \left(\frac{\gamma p_\infty}{\gamma - 1} \right) + \mathbf{u} \cdot \nabla \left(\frac{\gamma p_\infty}{\gamma - 1} \right) = 0. \quad (4)$$

Abgrall (1996) proved that a multi-component continuum scheme needs to satisfy Eq. (4.1) in the discrete sense to prevent unphysical oscillations at material boundaries. Although different scheme alterations are possible to satisfy this requirement, cf. Abgrall and Karni (2001), the utilization of (4) in the governing equations and therefore direct discretization together with (1) is the simplest remedy to the problem, cf. Shyue (1998) and Shyue (2006).

2.2 Finite volume scheme

The appropriate discretization technique for hyperbolic problems with discontinuities (shocks, material boundaries, etc.) is the finite volume approach. For simplicity, we restrict ourselves in the following to the two-dimensional case and assume an equidistant discretization with mesh widths Δx_1 , Δx_2 and a constant time step Δt . Since the equations (4) are not in conservation form, we use the Wave Propagation Method by LeVeque (2002) to discretize the system (1), (4). An explicit two-dimensional wave propagation scheme has the formal structure

$$\mathbf{Q}_{jk}^{l+1} = \mathbf{Q}_{jk}^l - \frac{\Delta t}{\Delta x_1} \left(\mathcal{A}^- \Delta_{j+\frac{1}{2},k} + \mathcal{A}^+ \Delta_{j-\frac{1}{2},k} \right) - \frac{\Delta t}{\Delta x_2} \left(\mathcal{B}^- \Delta_{j,k+\frac{1}{2}} + \mathcal{B}^+ \Delta_{j,k-\frac{1}{2}} \right).$$

While the *fluctuations* $\mathcal{A}^\pm \Delta$, $\mathcal{B}^\pm \Delta$ can be supplemented with (limited) second-order and cross-derivative contributions resulting in a truly multi-dimensional high-resolution Godunov-type method (LeVeque, 2002), the key component is an approximate Riemann solver that provides a linearized decomposition of the Riemann problem (RP) normal to each cell boundary. In here, we use the HLLC¹ approach by Toro et al. (1994) that is tailored specifically for the Euler equations and approximates the RP (here x_1 -direction) with three discontinuous jumps by

$$\mathbf{q}^{HLLC}(x_1, t) = \begin{cases} \mathbf{q}_l, & x_1 < s_l t, \\ \mathbf{q}_l^*, & s_l t \leq x_1 < s^* t, \\ \mathbf{q}_r^*, & s^* t \leq x_1 \leq s_r t, \\ \mathbf{q}_r, & x_1 > s_r t, \end{cases}$$

which is also depicted in Fig. 1. For the wave speeds $s_{l/r}$ we use the estimations $s_l = \min\{u_{1,l} - c_l, u_{1,r} - c_r\}$, $s_r = \max\{u_{1,l} + c_l, u_{1,r} + c_r\}$ suggested by Davis (1988) and s^* is given in the HLLC approach by

$$s^* = \frac{p_r - p_l + s_l u_{1,l} (s_l - u_{1,l}) - \rho_r u_{1,r} (s_r - u_{1,r})}{\rho_l (s_l - u_{1,l}) - \rho_r (s_r - u_{1,r})}.$$

Conservation arguments and consideration of the structure of the RP for Euler equations lead to the specification of the unknown solution values as

$$\mathbf{q}_k^* = \left[\eta, \eta s^*, \eta u_2, \eta \left[\frac{(\rho E)_k}{\rho_k} + (s^* - u_{1,k}) \left(s_k + \frac{p_k}{\rho_k (s_k - u_{1,k})} \right) \right], \frac{1}{\gamma_k - 1}, \frac{\gamma_k p_{\infty,k}}{\gamma_k - 1} \right]^T, \quad \eta = \rho_k \frac{s_k - u_{1,k}}{s_k - s^*}$$

for $k = \{l, r\}$, cf. Toro (1999). Knowledge of the intermediate state then allows the direct evaluation of the *waves* as $\mathcal{W}_1 = \mathbf{q}_l^* - \mathbf{q}_l$, $\mathcal{W}_2 = \mathbf{q}_r^* - \mathbf{q}_l^*$, $\mathcal{W}_3 = \mathbf{q}_r - \mathbf{q}_r^*$ and by setting $\lambda_1 = s_l$, $\lambda_2 = s^*$, $\lambda_3 = s_r$ the fluctuations in the x_1 -direction are defined as $\mathcal{A}^- \Delta = \sum_{\lambda_\nu < 0} \lambda_\nu \mathcal{W}_\nu$, $\mathcal{A}^+ \Delta = \sum_{\lambda_\nu \geq 0} \lambda_\nu \mathcal{W}_\nu$ for $\nu = \{1, 2, 3\}$.

Note that the robustness and positivity preservation of the HLLC approach is essential for obtaining reliable simulation results when multiple fluids with disparate material properties are involved as is the case in the computations presented in the Sections 6.2 and 6.3.

2.3 Numerical treatment of thin-walled structures

Geometrically complex moving boundaries are incorporated into the finite volume scheme by using some of the cells as ghost cells for enforcing immersed moving wall boundary conditions, cf. Arienti et al. (2003) and Fedkiw et al. (1999). The boundary geometry is mapped onto the Cartesian mesh by employing a scalar level set function ϕ that stores the distance to the boundary surface and allows the efficient evaluation of the boundary outer normal in every mesh point as $\mathbf{n} = -\nabla \phi / |\nabla \phi|$. Since, throughout this paper, we employ only thin-shell and beam solid mechanics solvers that discretize the structure with a topologically possibly open lower dimensional manifold surface mesh, we use *unsigned* distance as level set information and employ those fluid cells as exterior ghost cells for which the cell *midpoint* satisfies $\phi < h/2$.² The latter condition is a straightforward, unambiguous solution to achieve the mandatory thickening of the surface mesh by the element thickness h . The contour line $\phi = h/2$ effectively represents the embedded boundary for the fluid solver (depicted as dotted line around shell elements in Fig. 2). The hydrodynamic load on each thin element is then evaluated as the difference between the approximated pressure values at $\phi = h/2$ in the positive and negative direction of each element's normal, i.e. $p^F := p^+ - p^-$.

For the governing equations (1), the boundary condition at a rigid wall moving with velocity \mathbf{v} is $\mathbf{u} \cdot \mathbf{n} = \mathbf{v} \cdot \mathbf{n}$. Enforcing the latter with ghost cells, in which the discrete values are located at the cell centers, requires the mirroring of the values ρ , \mathbf{u} , p , $1/(\gamma - 1)$, and $\gamma p_\infty / (\gamma - 1)$ across the embedded boundary. The normal velocity in the ghost cells is set to $(2\mathbf{v} \cdot \mathbf{n} - \mathbf{u} \cdot \mathbf{n})\mathbf{n}$, while the mirrored tangential velocity remains unmodified. Mirrored values are constructed by calculating spatially interpolated values in the point $\tilde{\mathbf{x}} = \mathbf{x} + 2\phi\mathbf{n}$ from neighboring interior cells. We employ a dimension-wise

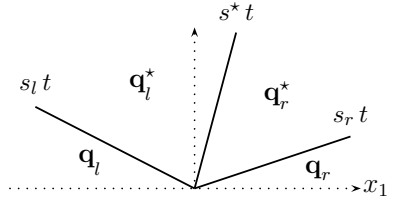


Figure 1: Approximation of the RP by the HLLC scheme.

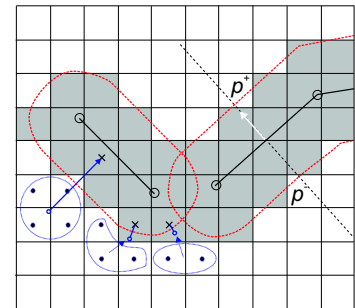


Figure 2: Ghost cells (shaded gray) around shell elements (dark segments) and construction of mirrored values.

¹HLLC:Harten-Lax-van Leer Riemann solver with restored Contact surface

²For topologically closed boundary surfaces it is also possible to use signed distance instead, cf. (Deiterding, 2006) and (Cirak and Radovitzky, 2005).

linear interpolation for this operation, but it has to be emphasized that directly near the boundary the number of interpolants needs to be decreased to ensure the monotonicity of the numerical solution. This property is essential in simulating hyperbolic problems with discontinuities. Figure 2 also highlights the necessary reduction of the interpolation stencil for some exemplary cases. The interpolation locations are indicated by the origins of the arrows normal to the contour line that defines the embedded boundary. After the application of the numerical scheme, cells that have been used to impose internal boundary conditions are set to the entire state vector of the nearest cell in the fluid interior. This operation ensures proper values in case such a cell becomes a regular interior cell in the next step due to boundary movement. The consideration of \mathbf{v} in the ghost cells also guarantees that the embedded boundary propagates at most one cell in every time step.

Note that the described technique does not require a modification of the numerical stencil itself and is therefore generically applicable, but causes a slight diffusion of the boundary location throughout the method and results in an overall non-conservative scheme. The boundary undergoes a staircase approximation that potentially can give rise to considerable errors in the computed solution. However, by refining the embedded boundary, typically up to the highest available resolution, with the dynamic mesh adaptation method described in next subsection, we alleviate these problems effectively. A refinement criterion based on $\phi \equiv 0$ has been implemented for this purpose.

2.4 Structured adaptive mesh refinement

In order to supply a fine local temporal and spatial resolution efficiently, we use the block-structured adaptive mesh refinement (SAMR) method by Berger and Colella (1988). Characteristic for the SAMR method is that a specific finite volume method is technically not implemented in a cell-based fashion, but rather in a routine operating on equidistant subgrids. The subgrids become computationally decoupled during one update cycle through the use of ghost or halo cells. Starting from the base mesh on level 0, the time step size and all spatial mesh widths on level $l > 0$ are r_l -times finer than on level $l - 1$ and a time-explicit finite volume scheme will (in principle) remain stable on all levels of the recursively nested refinement hierarchy. Ghost cell values at coarse-fine interfaces are constructed by interpolating coarse level data, which mandates a recursive order of update (cf. Sec. 5.1). SAMR in the VTF is provided generically by the AMROC (Adaptive Mesh Refinement in Object-oriented C++) framework (Deiterding, 2002) that can be used on all parallel systems that provide the MPI library.

3 Lagrangian thin-shell solver

The Kirchhoff-Love thin-shell model applied here for three-dimensional thin-shell simulation has been discretized with smooth subdivision finite elements, as previously described by Cirak and Ortiz (2001) and Cirak et al. (2000). Notably, the underlying kinematic assumptions allow for finite strains, displacements and rotations. The subdivision shell elements have also been extended to the range of applications that involve fracture and fragmentation, cf. Cirak et al. (2005). Thereby, fracture initiation and propagation is considered as a progressive failure phenomenon in which the separation of the crack flanks is modeled with a cohesive law. In the present implementation, cohesive interface elements are inserted at all inter-element edges and constrain the opening of the crack flanks to the deformation of the shell mid-surface and its normal.

3.1 Governing equations in weak form

To kinematically describe a possibly fractured thin-shell as sketched in Fig. 3(a), we first consider the shell in its undeformed configuration \bar{V} . The position vector $\bar{\varphi}$ of a material point on the undeformed shell $\bar{\varphi}$ of a material point on the undeformed shell body is assumed to be

$$\bar{\varphi} = \bar{\mathbf{x}} + \theta_3 \bar{\mathbf{n}} \quad (5)$$

with the uniform thickness \bar{h} and $-\bar{h}/2 \leq \theta_3 \leq \bar{h}/2$. The position vector of the shell mid-surface is denoted by $\bar{\mathbf{x}}$ and its out-of-surface unit normal by $\bar{\mathbf{n}}$. In other words, the shell mid-surface represents a two-dimensional manifold in \mathbb{R}^3 . The deformation mapping φ maps the shell body into the deformed configuration V

$$\varphi = \mathbf{x} + \theta_3 \lambda \mathbf{n} \quad (6)$$

where \mathbf{x} and \mathbf{n} are the deformed mid-surface and its normal. The thickness stretch parameter λ is the ratio of the deformed shell thickness h to the reference thickness \bar{h} . In the presence of a crack, the deformation is discontinuous across the crack and has a jump, i.e.

$$\llbracket \varphi \rrbracket = \varphi^+ - \varphi^- = \llbracket \mathbf{x} \rrbracket + \theta_3 \llbracket \mathbf{n} \rrbracket, \quad (7)$$

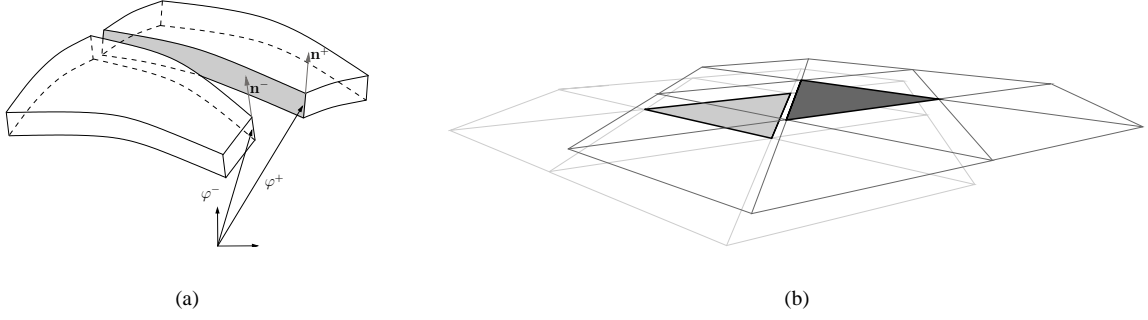


Figure 3: (a) Fractured shell body: opposite crack flanks and corresponding normals. (b) A cohesive edge and its two adjacent elements.

where the superscripts $+$ and $-$ refer to the opposing crack flanks. Further, the first term describes the discontinuity of the deformation of the shell mid-surface, and the second term the discontinuity in the shell out-of-surface normal. The discontinuities in the deformations can also be interpreted as the opening displacement of the crack. Further, note that the Kirchhoff-Love constraint is satisfied, i.e. $\mathbf{x} \cdot \mathbf{n} = 0$, on both sides of the crack.

A standard semi-inverse approach is followed for obtaining the shell equilibrium equations in weak form. To this end, the assumed reduced kinematic equations for the shell body (Equations (5) and (7)) are introduced into the conventional virtual work expression for the three-dimensional body. As previously mentioned, we consider fracture as a gradual separation phenomenon, resisted by cohesive tractions. Consequently, the internal virtual work expression contains the virtual work of the cohesive interface ($\delta\Pi_{C,int}$) in addition to the virtual work of the bulk material ($\delta\Pi_{S,int}$)

$$\delta\Pi_{S,int} + \delta\Pi_{C,int} - \delta\Pi_{ext} = 0 \quad (8)$$

with the external virtual work $\delta\Pi_{ext}$ and

$$\delta\Pi_{S,int} = \int_{\bar{\Omega}} \int_{-\bar{h}/2}^{\bar{h}/2} \mathbf{P} : \delta\mathbf{F} \mu d\theta^3 d\bar{\Omega}, \quad \delta\Pi_{C,int} = \int_{\bar{\Gamma}_C} \int_{-\bar{h}/2}^{\bar{h}/2} \mathbf{T} \cdot \llbracket \varphi \rrbracket \mu d\theta^3 d\bar{\Gamma}_C,$$

where \mathbf{P} is the first Piola-Kirchhoff stress tensor, \mathbf{T} is the related traction vector at the cohesive surface, and \mathbf{F} is the deformation gradient. The virtual work expression for the bulk material is integrated over the undeformed shell mid-surface $\bar{\Omega}$ and for the cohesive interface over the crack path $\bar{\Gamma}_C$. The scalar factor μ accounts for the curvature of the shell in the volume computation, cf. Cirak and Ortiz (2001).

3.2 Subdivision thin-shell elements

Next, we briefly outline the discretization of the governing equation (8) firstly for the non-fractured case. A detailed presentation of the used subdivision finite element discretization technique can be found in (Cirak et al., 2000) and (Cirak and Ortiz, 2001). In this approach, the reference ($\bar{\mathbf{x}}$) and deformed (\mathbf{x}) shell surfaces are approximated using smooth subdivision surfaces belonging to the Sobolev space H^2 with square-integrable curvatures. The subdivision interpolation within one element is accomplished with shape functions, which have support on the element as well as on the one-ring of neighboring elements. The overlapping local subdivision interpolants, each defined over one patch, together lead to a global interpolant with square-integrable curvatures. Importantly, smoothness is achieved without introducing nodal rotations as degrees of freedom. The absence of nodal rotations is particularly appealing in the presence of finite rotations.

In the presence of fracture, the smoothness and/or continuity of the interpolation has to be relaxed and the subdivision interpolant needs to be modified, cf. Cirak et al. (2005). The topological changes necessary to the non-local subdivision functions and the underlying control mesh in order to describe the dynamic propagation of a single crack are complicated. Therefore, we chose to pre-fracture the element patches, such that each patch possesses its own nodes and acts independently for the purpose of interpolation, see Fig. 3(b). Prior to crack nucleation, the coupling of the elements is enforced by applying stiff elastic cohesive interfaces at all edges. Once fracture nucleates along an element edge, the element patches on both sides of the cracked edge interact through cohesive tractions. The cohesive tractions are self-balanced internal forces derived from a cohesive fracture model.

3.3 Constitutive models for the shell

An irreversible cohesive constitutive model as proposed by Ortiz and Pandolfi (1999) is used for modeling the cracks. Thereby, the opening displacement $\llbracket\varphi\rrbracket$ plays the role of a deformation measure while the traction \mathbf{T} is the conjugate stress measure. Further, a scalar effective opening displacement is defined by

$$\delta = \sqrt{\beta^2 |\delta_t|^2 + |\delta_n|^2},$$

where δ_t and δ_n are the tangential and normal displacement components of $\llbracket\varphi\rrbracket$ with respect to the crack surface. The parameter β assigns different weights to the tangential and normal opening displacements. The cohesive tractions \mathbf{T} are given by

$$\mathbf{T} = \frac{t}{\delta} (\beta^2 \delta_t + \delta_n).$$

The scalar effective traction t is computed from a cohesive law as shown in Fig. 4. In addition to the parameter β , the model parameters are the maximal tensile stress σ_c and the critical opening displacement δ_c . The following relationship between the cohesive law and the critical fracture energy rate G_c exists:

$$G_c = \int_0^\infty t d\delta$$

which can be used for determining δ_c . For further details see Ortiz and Pandolfi (1999).

The inelastic behavior of the bulk material, i.e. the relation between \mathbf{P} and \mathbf{F} , is described with a conventional J_2 viscoplasticity model with isotropic power-law hardening as described by Cuitino and Ortiz (1992). The power-law hardening for the flow stress g has the form

$$g(\epsilon^p) = \sigma_y \left(1 + \frac{\epsilon^p}{\epsilon_0^p} \right)^{1/n},$$

where σ_y is the initial yield stress, ϵ^p and ϵ_0^p are the total and the reference plastic strains, respectively, and $1/n$ is the hardening exponent. The rate-dependent behavior is described in terms of the effective von Mises stress σ_{eff} with a power viscosity law and constant rate sensitivity

$$\sigma_{\text{eff}} = g(\epsilon^p) \left(1 + \frac{\dot{\epsilon}^p}{\dot{\epsilon}_0^p} \right)^{1/m},$$

where $\dot{\epsilon}_0^p$ is the reference plastic strain rate and $1/m$ the strain rate sensitivity exponent.

The thin-shell typical plane stress condition is enforced with a local Newton-Raphson iteration at each quadrature point, cf. deBorst (1991). Thereby, the thickness stretch parameter λ (Eq. 6) is the unknown variable in the iteration.

4 Efficient level set evaluation

In Section 2, we have sketched the concept of employing a distance function to represent a complex embedded boundary on a Cartesian mesh. While distance functions are easily prescribed for single elementary geometric objects, their evaluation can be cumbersome for complex shapes. In coupled Eulerian-Lagrangian simulations, this complex shape is defined by the deforming shell surface mesh.

One can efficiently compute the distance on a grid by solving the eikonal equation with the method of characteristics and utilizing polyhedron scan conversion, cf. Mauch (2003). For a given grid point, the relevant closest point on the triangular mesh lies on one of the primitives (faces, edges and vertices) that comprise the surface. The characteristics emanating from each of these primitives form polyhedral shapes. Such a *characteristic polyhedron* contains all of the points which are possibly closest to its corresponding face, edge or vertex. The closest points to a triangle face must lie within a triangular prism defined by the face and its normal; the closest points to an edge

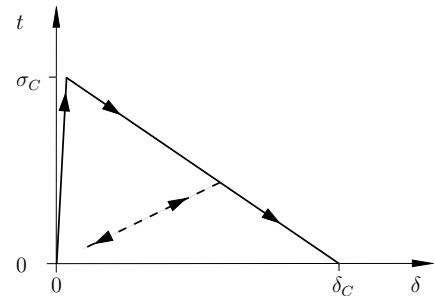


Figure 4: Irreversible linear cohesive law. Note that the initial stiff elastic response enforces the displacement continuity prior to crack initiation at σ_c . The dashed line represents the loading-unloading rule.

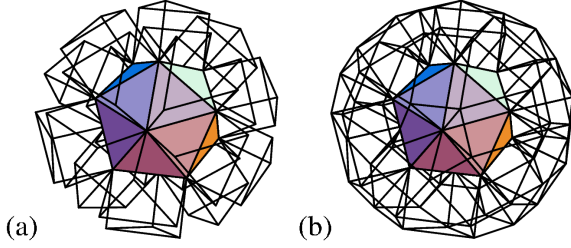


Figure 5: The characteristic polyhedra for faces and edges of an icosahedron.

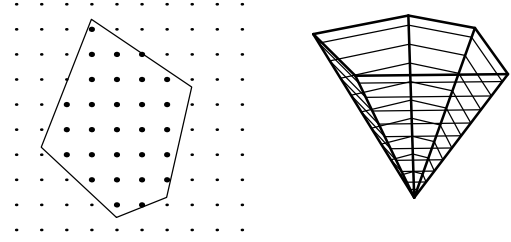


Figure 6: Slicing of a polyhedron to form two-dimensional polygons (right) and scan conversion of an exemplary case (left).

lie in a cylindrical wedge defined by the line segment and the normals to the two incident faces (see Fig. 5 for face (a) and edge (b) polyhedra for a particular example). Analogously, polygonal pyramids emanating from the vertices are also possible (not shown). We then determine the grid points that lie inside a characteristic polyhedron with polyhedron scan conversion. The polyhedron is first sliced along each sheet of the grid lattice to produce polygons, cf. Fig. 6. Simple geometric formulas are finally used to calculate the distance once a polyhedron has been assigned uniquely to each grid point.

By utilizing the outlined techniques, and evaluating the distance exactly only within a small distance around the surface, a highly efficient algorithm can be formulated that has linear computational complexity both in the number of Cartesian mesh points and the surface triangles, cf. Mauch (2003) and Deiterding et al. (2006c).

5 Fluid-structure coupling

The explicit fluid and solid solvers are weakly coupled by successively applying appropriate boundary conditions in a time-operator splitting technique. In the case of inviscid flows, the compatibility conditions are the continuity of the velocity component normal to the embedded boundary u_n in solid (S) and fluid (F), i.e. $u_n^S = u_n^F$, and the continuity of the normal component of the solid's Cauchy traction vector, $p^S = (\sigma \mathbf{n}) \mathbf{n}$ with $\sigma = 1/\det(\mathbf{F}) \mathbf{F} \mathbf{P}$, and the hydrodynamic pressure p^F , i.e. $p^S = p^F$. We use the following update algorithm to implement these coupling conditions numerically:

```

update  $\phi(t)$ 
 $\mathbf{v}_F^{+/-} := \mathbf{u}^S(t)$ 
update_fluid( $\Delta t$ )
 $p^S := p^F(t + \Delta t)$ 
update_solid( $\Delta t$ )
 $t := t + \Delta t$ 

```

After evaluating the distance function ϕ for the currently available shell surface mesh, the embedded wall boundary velocities for the fluid solver are set to the solid velocities in the nearest shell element midplane. The same velocity \mathbf{v} is enforced in the fluid on upper (+) and lower (-) side of each element. After setting embedded rigid wall boundary conditions and the fluid update, a new hydrodynamic pressure load $p^F := p^+ - p^-$ on each shell element (compare Fig. 2) is derived by evaluating p^\pm with the linear interpolation / extrapolation operation already sketched in Section 2.3. With these new boundary conditions, the cycle is completed by advancing the solid by Δt , which in practice is typically done by taking multiple, smaller time steps in the solid solver to effectively accommodate the more restrictive stability condition in the solid.

5.1 Application of SAMR in the fluid solver

While the implementation of a loosely coupled FSI method is straightforward with conventional solvers with consecutive time update, the utilization of the recursive SAMR method with hierarchical time step refinement in the fluid is non-apparent. In the VTF, we treat the fluid-solid interface as a discontinuity that is a-priori refined at least up to a coupling level l_c . The resolution at level l_c has to be sufficiently fine to ensure an accurate wave transmission between fluid and structure, but might not be the highest level of refinement. To incorporate the fluid-structure data exchange into the recursive SAMR algorithm it has to be ensured that the updated mesh positions and nodal velocities are received *before* a regridding of the coupling level l_c is initiated and that the hydrodynamic pressure loadings

on the interface are evaluated *after* the highest available refinement level has reached the same discrete time as the updated level l_c . We visualize the data exchange between solid and SAMR fluid solver in Fig. 7 for an exemplary SAMR hierarchy with two additional levels with $r_{1,2} = 2$. Figure 7 pictures the recursion in the SAMR method by numbering the fluid update steps (F) according to the order determined by the SAMR method. The order of the solid update steps (S) on the other hand is strictly linear. The red diagonal arrows correspond to the sending of the interface pressures p^F from fluid to solid at the end of each time step on level l_c . The blue upward arrows visualize the sending of the interface mesh and its nodal velocities \mathbf{u}^S after each solid update. The modification of refinement meshes is indicated in Fig. 7 by the gray arrows; the initiating base level, that remains fixed throughout the regridding operation, is indicated by the gray circles.

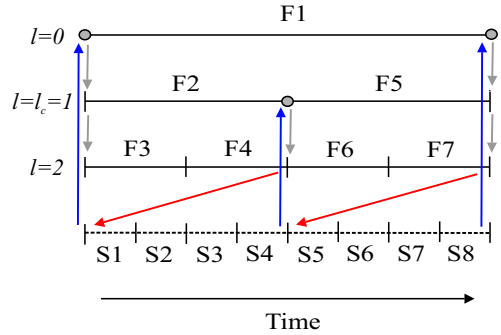


Figure 7: Data exchange between the recursive fluid solver and the linear thin-shell solver during one SAMR root level time step.

5.2 Software implementation

The fluid-structure coupling software VTF is a collection of C++ classes for implementing high-speed FSI problems on distributed memory machines. At present, only the loose coupling of time-explicit solvers is supported. The design follows a classical framework approach in which the instantiation of the main objects is usually done in a short generic main program and customization is achieved through subclass derivation.

In our current implementation, computational fluid and solid dynamics solvers are parallelized separately for distributed memory machines using independent rigorous domain decomposition methods. In order to facilitate an efficient communication of the distributed fluid-shell boundary information we have implemented a non-blocking high-level communication library that determines the necessary point-to-point communication patterns by intersecting Cartesian bounding boxes enclosing the local domains. Details on this communication library and also a detailed algorithmic description of the coupled SAMR method can be found in (Deiterding et al., 2006c).

6 Computational results

In the following sub-sections, we consider three different configurations to demonstrate the versatility of our fluid-structure coupling approach. While Section 6.1 discusses a verification test of linearly elastic motion due to the impact of a shock wave in air, the computations in Sections 6.2 and 6.3 simulate viscoplastic deformation and fracture driven by strong pressure waves in water. In both cases the induced solid motion causes tension in the liquid that results in cavitation when the pressure falls below the water vapor pressure. Since cavitation inception limits the maximal tension, and thereby the minimal pressure the liquid can support, we employ an additional pressure cutoff model (see also Xie et al. (2006)) in these computations. It is implemented by applying the non-conservative energy correction

$$E := \frac{p_c + \gamma p_\infty}{\rho(\gamma - 1)} + \frac{1}{2} \mathbf{u}^T \mathbf{u}, \quad \text{for } p < p_c \quad (9)$$

after every fluid time step and its purpose is to limit all hydrodynamic pressures to the cutoff value p_c .

6.1 Verification

As a first test for the coupled method, we consider the verification configuration of a thin-walled steel panel impacted by a planar shock wave in air ($\gamma^A = 1.4$, $p_\infty^A = 0$) proposed by Giordano et al. (2005). The panel has the thickness $h = 1$ mm and extends 50 mm from a mounting with forward-facing step geometry into which it is firmly clamped. Figure 8 depicts the computational domain and initial conditions. Inflow boundary conditions are applied on the left side, rigid wall boundary conditions anywhere else.

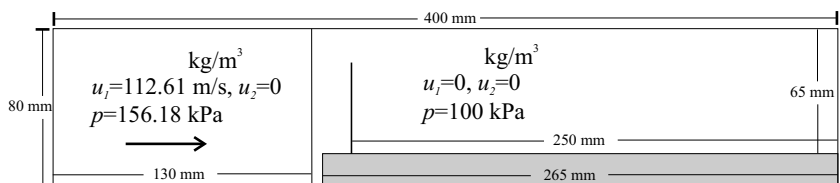


Figure 8: Geometry of the computational setup for the shock-panel test case.

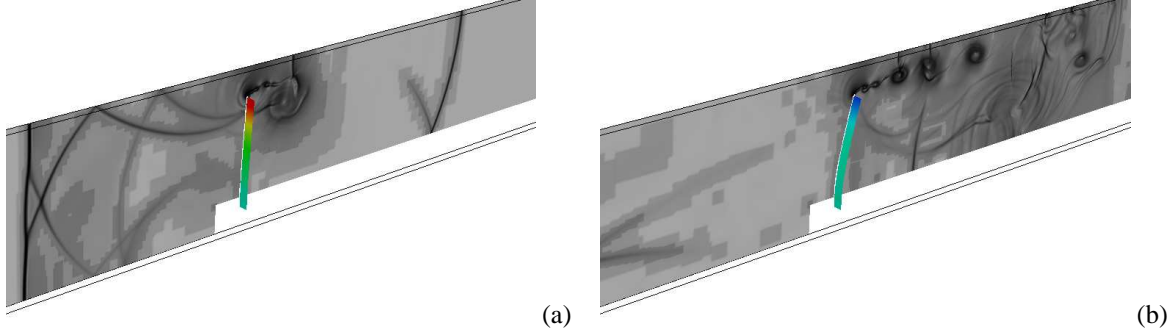


Figure 9: Snapshots at $t = 0.43$ ms (a) and $t = 1.56$ ms (b) visualize the evolution of the fluid mesh adaptation (different levels indicated by gray scales) according to the flow field and the deflection of the thin-shell panel.

First, we model the panel as a one-dimensional elastic beam immersed into a two-dimensional fluid domain and solve the Euler-Bernoulli beam equation

$$\rho_s h \frac{\partial^2 w}{\partial t^2} + EI \frac{\partial^4 w}{\partial \bar{x}^4} = p^F \quad (10)$$

for $\rho_s = 7600$ kg/m³, $E = 220$ GPa, and $I = h^3/12$ to calculate the deflection $w(\bar{x}, t)$ of the beam middle axis with updated hydrodynamic loading p^F after every time step of the fluid solver. Equation (10) is approximated with a straightforward time-implicit finite difference approach and the resulting linear system is solved by QR decomposition. An equidistant mesh of 101 points is used to discretize the beam middle axis. The fluid mesh uses a base grid of 320×64 cells and allows up to two additional levels of dynamic isotropic refinement (based on ϕ and scaled gradients of ρ and p) with refinement factors $r_{1,2} = 2$. Calculating 18,660 coupled time steps at $l_c = 2$ to $t_e = 5.0$ ms required ~ 12.3 h CPU on a 3.4 GHz processor.

Second, the panel is modeled as a two-dimensional plate strip of 5 mm width (325 triangular elements) and embedded into a three-dimensional fluid base mesh of $320 \times 64 \times 2$ cells. The structural motion is computed with the previously described three-dimensional thin-shell finite element solver. Linear elastic material behavior with the parameters given above and the Poisson ratio $\nu = 0.3$ is assumed. Figure 9 shows the dynamic bending of the plate strip and the evolving fluid mesh adaptation with two additional levels (depicted by gray scales) as the initial shock is partially reflected (a) and increased vortex shedding occurs at the panel tip (b). The three-dimensional computation reached $t_e = 5.0$ ms after 18,000 coupled time steps, where 5 solid solver sub-steps were used, and required ~ 322 h CPU.

A comparison of the predicted panel tip displacement versus time for both FSI simulations is given in Fig. 10. Slight divergences at later times are expectable considering the apparent differences in beam and shell theory. However, both FSI configurations show excellent agreement at earlier times and are in proximity to a-priori predictions based on Eq. (10) alone (Beam) for the constant instantaneous loading $p^F \equiv 100$ kPa that has been found to be a rough approximation for the pressure loading for approximately $t < 2.5$ ms, cf. Giordano et al. (2005).

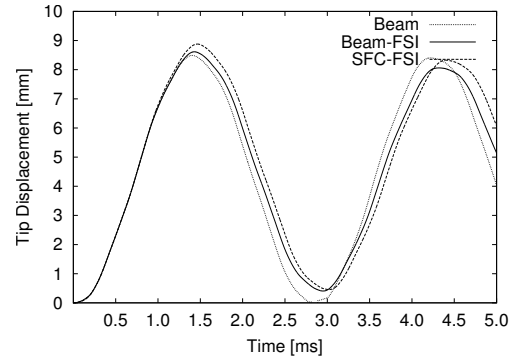


Figure 10: Tip motion for both FSI computations and reference computation with constant loading.

6.2 Underwater explosion

As a first test for shock waves in water, we simulate a fluid-structure experiment by Ashani and Ghamsari (2008). A small charge ($m_{C4} = 20$ g and $m_{C4} = 30$ g) of the explosive C4 ($1.34 \times$ TNT) is detonated in a water-filled basin at the standoff distances $d = 25$ cm or $d = 30$ cm above a circular air-backed aluminum plate (exposed radius 85 mm) of thickness $h = 3$ mm. We model the basin with a fluid domain of $2 \text{ m} \times 1.6 \text{ m} \times 2 \text{ m}$, where the origin is placed at the domain center. Outflow is assumed at all domain boundaries. In analogy to the experiment, air-backed conditions are represented by inserting a rigid cylinder of radius 150 mm from $x_2 = -0.8$ m to $x_2 = 0$ into the domain. The cylinder is sealed by the test plate of radius 150 mm, discretized with 8148 triangles, which is treated as rigid for $r > 85$ mm. The material parameters for viscoplastic material behavior of aluminum, that were used in these simulations, are detailed in Table 1. It is assumed that the aluminum is strain-rate insensitive

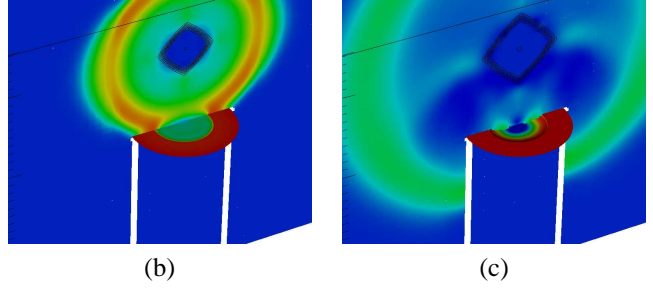
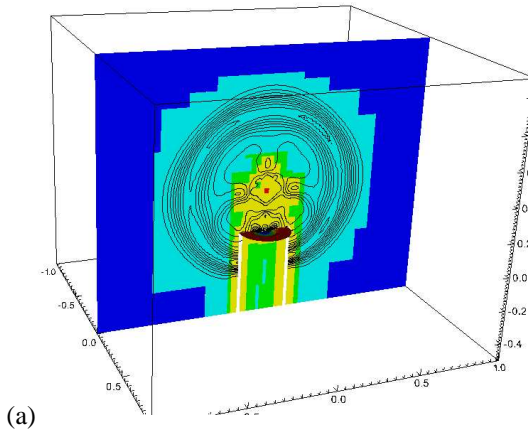


Figure 11: (a) Isolines of p on domains of refinement levels (indicated by color) at $t = 0.31$ ms. (b), (c) The plane shows a color plot of p and isolines of α^A , the plate displays the normal vertex velocity at $t = 0.14$ ms and 0.31 ms.

and strain-softening effects have not been considered. The cylinder is filled with air ($\gamma^A = 1.4, p_\infty^A = 0$) at density $\rho^A = 1.29 \text{ kg/m}^3$, the basin with water ($\gamma^W = 7.415, p_\infty^W = 296.2 \text{ MPa}$) at $\rho^W = 1027 \text{ kg/m}^3$, which are both initially at rest and assumed to be at atmospheric pressure $p_0 = 100 \text{ kPa}$ (the static pressure increase due the water depth can safely be neglected). The modification by Eq. (9) with $p_c = -1 \text{ MPa}$ is employed in the fluid solver to consider cavitation inception. The shock from the explosion is modeled as a spherical energy deposition ($m_{C4} \cdot 6.06 \text{ MJ/kg}$) uniformly distributed over a sphere of radius 5 mm of air at temperature 1500°C located at $(0, d, 0)$.

The fluid domain is discretized with an SAMR base mesh of $50 \times 40 \times 50$ cells. Four additional levels with refinement factors $r_{1,2,3} = 2, r_4 = 4$ are employed. The highest level refinement is static and restricted to the explosion center. Fluid mesh adaptation on all other levels is dynamic and based on ϕ and the scaled gradient of p . However, refinement at levels 2 and 3 is restricted to the immediate vicinity of the structure and the shock as it impinges onto it. Figure 11(a) depicts a snapshot of the fluid mesh in a plane through the center of the domain for the case $m_{C4} = 20 \text{ g}, d = 25 \text{ cm}$. The FSI simulation uses $l_c = 3$ with 2 solid solver sub-steps, and 1296 coupled time steps were computed to reach the final time $t_e = 1 \text{ ms}$.

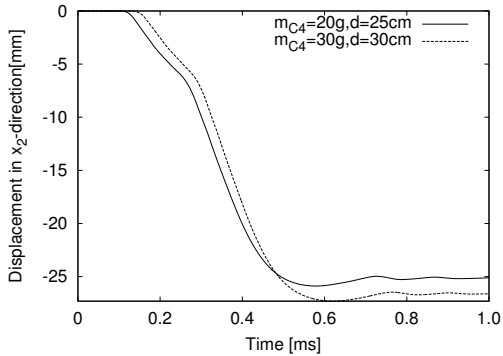


Table 1: Material properties for aluminum.

Mass density	$\rho_s = 2719 \text{ kg/m}^3$
Young's modulus	$E = 69 \text{ GPa}$
Poisson's ratio	$\nu = 0.33$
Yield stress	$\sigma_y = 217.6 \text{ MPa}$
Reference plastic strain	$\epsilon_0^p = 0.025$
Hardening exponent	$1/n = 0.6$
Rate sensitivity exponent	$1/m = 0$

Figure 12: Left: center displacement versus time.

The impact of the spherical shock onto the plate and its partial reflection are visualized in graphics (b) and (c) of Fig. 11, respectively. The induced motion of the exposed part of the test specimen is clearly visible. Figure 12 displays the plate center motion versus time for both cases considered. Note that during the first $\sim 0.2 \text{ ms}$ after the shock impact the deformation occurs with constant velocity since the water near the plates cavitates and does not transmit significant forces onto the plate. The maximal computed deflection for the case $m = 20 \text{ g}, d = 25 \text{ cm}$ is 25.88 mm , for the case $m_{C4} = 30 \text{ g}, d = 30 \text{ cm}$ it is 27.31 mm . Those values compare reasonably well to the experimental measurements of 28.83 mm and 30.09 mm by Ashani and Ghamsari (2008), where the differences are primarily due to our rather simplistic modeling of the initial shock wave created by the explosion. Both computations were run on 12 nodes of a parallel cluster with Intel-3.4 GHz-Xeon dual processors (10 nodes fluid, 2 nodes solid dynamics solver) and required $\sim 130 \text{ h CPU}$ each ($\sim 5.4 \text{ h wall time}$).

6.3 Plate deformation from water hammer

The final configuration considered is an experimental setup developed by Deshpande et al. (2006) that reproduces loading conditions of large-scale underwater explosions in the laboratory. By firing a steel projectile onto a piston

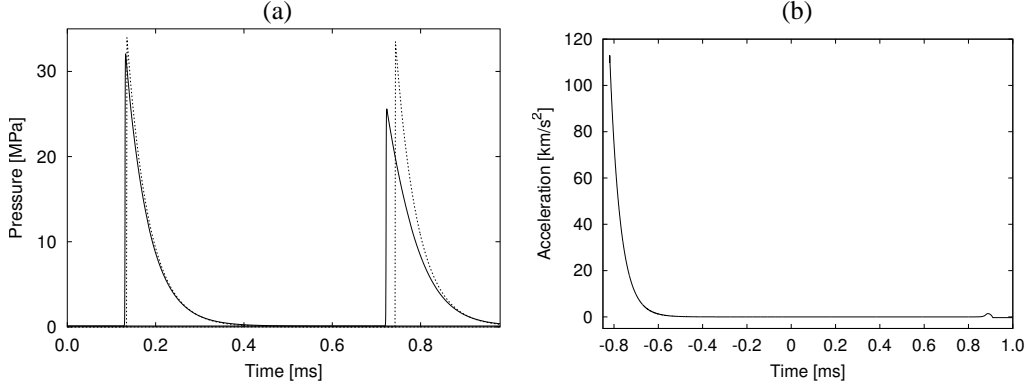


Figure 13: Loading conditions for $p_{\max} = 34$ MPa. (a) Comparison of the traveling wave approximation Eq. (12) (dotted) with computed pressure traces (solid) at $x_1 = 1.1$ m (left) and $x_1 = 0.2$ m (right). (b) Computed piston acceleration for the entire simulation time.

inserted into the end of a water shock tube, a strong pressure wave is created that propagates through the water column and impinges onto a circular copper plate sealing the other end. The shock tube has a length of 1.3 m and a radius of 32 mm, which is modeled with an additional signed distance level set function. The tube is filled with water ($\gamma^W = 7.415$, $p_\infty^W = 296.2$ MPa, $p_c = 0$) of density $\rho^w = 1000$ kg/m^3 at atmospheric pressure $p_0 = 101.3$ kPa. The copper plate has a thickness of 0.25 mm and a radius of $r = 56$ mm, but is unconstrained only for $r < 32$ mm. Again, the plate is air-backed ($\rho^A = 1.0$ kg/m^3 , $\gamma^A = 1.4$, $p_\infty^A = 0$) at pressure p_0 . The center of the plate is initially located at the coordinate origin and the shock tube middle axis is aligned with the x_1 -axis.

Verification of loading conditions

The motion of the piston creates a quasi one-dimensional pressure spike with exponential decay rate that propagates through the water column. We incorporate the piston movement into the computational setup by employing a second signed distance level set function that corresponds to the piston boundary in contact with the fluid. The level set is initially positioned at $x_1 = 1.3$ m and assumed to move with constant velocity b_0 . During a simulation, we integrate the law of motion for the piston

$$\bar{m}\dot{b} = -(\bar{p} - p_0) \quad (11)$$

with the forward Euler method and update level set position and velocity b in direction of the tube middle axis (to be used as wall normal velocity v_n for this level set, cf. Sec. 2.3) in every time step. As the piston is constrained in all other directions, it suffices to consider the hydrodynamic pressure averaged across the piston boundary \bar{p} and to use the averaged piston mass per unit area \bar{m} . In all subsequent computations the value $\bar{m} = 74.1$ kg/m^2 was used.

By assuming the wave to propagate with the constant speed of sound in water $c^w = 1482$ m/s , a traveling wave solution of the form

$$p(x_1, t) = \begin{cases} p_{\max} \exp\left(-\frac{t - x_1/c^w}{\bar{m}/(\rho^w c^w)}\right) & , \quad t \geq \frac{x_1}{c^w} \\ 0 & , \quad \text{otherwise} \end{cases} \quad (12)$$

can be derived for the pressure evolution at a fixed spatial location that is found to be in reasonable agreement with experimental measurements close to the piston boundary (Deshpande et al., 2006). The maximum of the traveling wave is set to $p_{\max} = \rho^w c^w b_0$, which permits the computation of the initial piston velocity b_0 for given p_{\max} . Plot (a) of Fig. 13 compares Eq. (12) evaluated at the locations $x_1 = 1.1$ m and $x_1 = 0.2$ m with pressure traces derived from a one-dimensional unigrid finite volume simulation with 2700 cells on the domain $[0 \text{ m}, 1.35 \text{ m}]$ for $p_{\max} = 34$ MPa. The agreement at early times is very good, verifying the correctness of our computational setup. At later times, the simulation necessarily differs from the unaltered (non-dispersive) traveling wave, because our computational model considers the density rise in the compression wave and the resulting change of the speed of sound. Plot (b) of Fig. 13 displays the computed piston acceleration, where the time is shifted by -0.82 ms setting the start of the FSI simulations to $t = 0$.

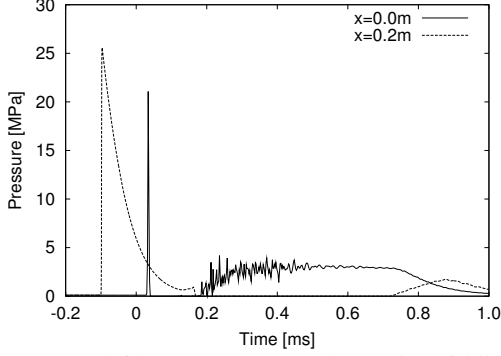


Figure 14: Fluid pressure traces along tube middle axis at $x_1 = 0$ and $x_1 = 0.2$ m for $p_{\max} = 34$ MPa.

Table 2: Material and cohesive model parameters for annealed copper.

Mass density	$\rho_s = 8920 \text{ kg/m}^3$
Young's modulus	$E = 130 \text{ GPa}$
Poisson's ratio	$\nu = 0.31$
Yield stress	$\sigma_y = 38.5 \text{ MPa}$
Reference plastic strain	$\epsilon_0^p = 0.0091$
Hardening exponent	$1/n = 0.627$
Reference plastic strain rate	$\dot{\epsilon}_0^p = 1000$
Rate sensitivity exponent	$1/m = 1.0$
Maximal tensile stress	$\sigma_c = 525 \text{ MPa}$,
Critical opening displacement	$\delta_c \approx 0.3 \text{ mm}$
Tangential weight parameter	$\beta^2 = 0.8$

Fluid-structure interaction simulations

While the thin copper plate exhibits just viscoplastic deformation for $p_{\max} = 34$ MPa, fracture occurs for larger values of p_{\max} . All computations were therefore run with activated cohesive interface element capability of the thin-shell solver. The parameters for the J_2 plasticity and the cohesive interface model used for annealed copper are given in Table 2. The mesh for the plate considers the mounting holes for purely optical reasons and consists of 8896 triangles. In order to ensure the correct boundary conditions throughout the whole simulation, the three-dimensional fluid domain covers with $[-0.146 \text{ m}, 1.35 \text{ m}] \times [-0.04 \text{ m}, 0.04 \text{ m}] \times [-0.04 \text{ m}, 0.04 \text{ m}]$ the entire shock tube.

To concentrate the computational resources for the fluid in the region of interest, the computation uses an SAMR base mesh of $374 \times 20 \times 20$ cells and two additional levels with refinement factors $r_{1,2} = 2$. The fluid mesh is always fully refined along the plate boundary and at the front of the incoming pressure wave. The shock tube boundary is statically refined at level 2 for $x_1 < 0.206$ m and at level 1 for $x_1 < 0.43$ m. The coupling level for the fluid-structure data exchange is set to $l_c = 2$. The simulations were run on 12 nodes of a parallel cluster consisting of Intel-3.4 GHz-Xeon dual processors CPUs, where 6 nodes were employed for the fluid and the solid solver, respectively. Using 2 solid solver sub-steps the case $p_{\max} = 34$ MPa took 4120 coupled time steps to reach $t_e = 1.0$ ms, which required ~ 48 h wallclock time (~ 1150 h CPU).

Results from the non-rupture case are displayed in the Figs. 14 and 15. Figure 14 shows pressure traces along the tube middle axis at the locations $x_1 = 0.2$ m and $x_1 = 0$. The impact of the pressure wave onto the plate at $t \approx 0.03$ ms and the water cavitation immediately after can be clearly inferred. An expansion wave due to the resulting structural motion travels upstream through the water column inducing a small piston acceleration around $t = 0.9$ ms, cf. Fig. 13(b).

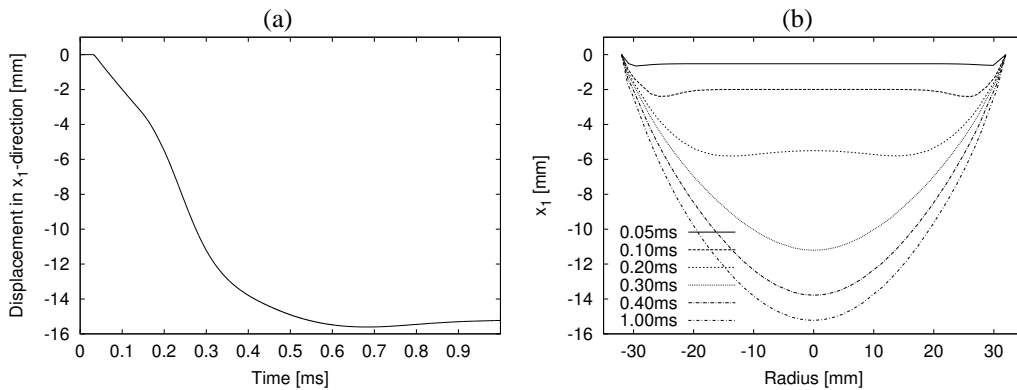


Figure 15: (a) Plate center displacement versus time and (b) deflection history of the plate midplane during the coupled simulation.

Similarly to the previous section, the plate deformation is separated into two phases. As can be seen in Fig. 15(a) cavitation leads to a constant displacement velocity during the first ~ 0.15 ms. The deflection of the plate is characterized by the appearance of a stationary plastic hinge at the boundary and a second instationary plastic hinge traveling towards the plate center, cf Fig. 15(b). Shortly after the fluid expansion wave leaves the plate

boundary, a hydrodynamic pressure of ~ 4 MPa builds up again directly at the plate until it declines finally from $t \approx 0.76$ ms on, cf. Fig. 14. During this phase, the plate deformation is nonlinear and the plate deflection is convex. The displacement reaches its maximum at $t \approx 0.76$ ms and remains almost unaltered until the end of the simulation at $t_e = 1.0$ ms. A visual comparison of the finally deformed solid mesh in the FSI simulation with a photograph of a target plate by Deshpande et al. is given in Fig. 16. The agreement is apparently very good. The obtained maximum deflection of 15.6 mm is also in good agreement with the analytic estimate of 16.1 mm by Qui et al. (2004) (Equation 21a in (Qui et al., 2004)). Note that Qui et al.'s estimate is for an ideally plastic material. In contrast, the presented computations include a strain-hardening effect, which has a reducing effect on the maximum displacements. Further, Qui et al. base their analysis on the traveling wave (12) that overpredicts the pressure maximum exposed to the plate, cf. Fig. 13(a).

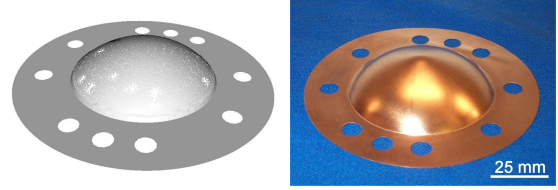


Figure 16: Comparison of simulated specimen with the experiment for $p_{\max} = 34$ MPa.

We present two exemplary results for plate rupture. When p_{\max} is moderately increased, the plate first bulges severely but then undergoes localized cracking at the plate center. This failure mode is shown in Fig. 17(a) for $p_{\max} = 64$ MPa that displays the situation at $t = 0.85$ ms simulation time when the fracture pattern is clearly established and the water splashes into the air behind the plate. Note also the similarity in longitudinal cracking behavior in simulation and experiment. When the loading is increased further, rupture occurs primarily at the supports. We display only one case for the high loading $p_{\max} = 173$ MPa that clearly exhibits tearing at the support from the initial impulse, cf. Fig. 17(b). Finally, it is worth mentioning that the reliable simulation of cracking phenomena with two coupled explicit solvers mandatorily requires a careful computational analysis of the stability condition in each sub-solver after every time step, which in our case also considers the temporal recursion in the SAMR approach. See Deiterding et al. (2006c) for details.

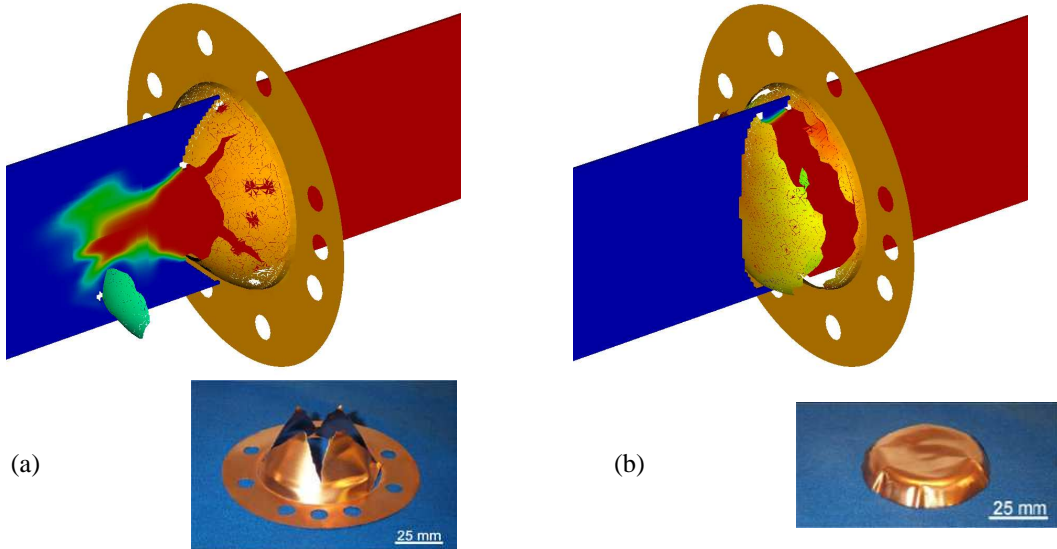


Figure 17: Plate fracture for $p_{\max} = 64$ MPa at $t = 0.85$ ms (a) and $p_{\max} = 173$ MPa at $t = 0.177$ ms (b), when the fracture patterns are fully established. The color midplane showing the volume fraction α^W in the fluid visualizes the water splash.

7 Conclusions

We have presented all computational components of a level-set-based fluid-structure coupling approach for the time-accurate simulation of thin flexible shells responding dynamically to strong pressure waves in water. The approach has been demonstrated to handle arbitrarily evolving thin-shells surrounded by fluid without problems. Three different fluid-structure interaction configurations of increasing complexity have been given to verify and validate the approach. The obtained results are found to be in good to excellent agreement with experimental observations, depending on the level of effort spent to reproduce the hydrodynamic loading conditions and to carefully adjust material model parameters that cannot be deduced unambiguously from tabulated data, namely for

viscoplasticity and fracture. The level of detail given should allow the easy reproducibility of our results thereby proving good verification tests for explicit FSI software. The integrated implementation of all presented components, including further documented explicit FSI testcases, is freely available from <http://www.cacr.caltech.edu/asc>.

Acknowledgements

We thank Vikram S. Deshpande from the Department of Engineering of the University of Cambridge for providing the plate photographs shown in the Figs. 16 and 17.

R. D. is sponsored by the Office of Advanced Scientific Computing Research, U.S. Department of Energy. All computations were performed at the Oak Ridge National Laboratory, which is managed by UT-Battelle, LLC under Contract No. DE-AC05-00OR22725.

References

- Abgrall, R.: How to prevent pressure oscillations in multicomponent flow calculations: A quasi conservative approach. *J. Comput. Phys.*, 125, (1996), 150–160.
- Abgrall, R.; Karni, S.: Computations of compressible multifluids. *J. Comput. Phys.*, 169, (2001), 594–523.
- Aivazis, M.; Goddard, W.; Meiron, D.; Ortiz, M.; Pool, J.; Shepherd, J.: A virtual test facility for simulating the dynamic response of materials. *Comput. Science & Engineering*, 2, 2, (2000), 42–53.
- Arienti, M.; Hung, P.; Morano, E.; Shepherd, J. E.: A level set approach to Eulerian-Lagrangian coupling. *J. Comput. Phys.*, 185, (2003), 213–251.
- Ashani, J. Z.; Ghamsari, A. K.: Theoretical and experimental analysis of plastic response of isotropic circular plates subjected to underwater explosion loading. *Mat.-wiss. u. Werkstofftechn.*, 39, 2, (2008), 171–175.
- Berger, M.; Colella, P.: Local adaptive mesh refinement for shock hydrodynamics. *J. Comput. Phys.*, 82, (1988), 64–84.
- Cirak, F.; Ortiz, M.: Fully c^1 -conforming subdivision elements for finite deformation thin-shell analysis. *Int. J. Numer. Meth. Engineering*, 51, (2001), 813–833.
- Cirak, F.; Ortiz, M.; Pandolfi, A.: A cohesive approach to thin-shell fracture and fragmentation. *Computer Methods in Appl. Mechanics and Engineering*, 194, (2005), 2604–2618.
- Cirak, F.; Ortiz, M.; Schröder, P.: Subdivision surfaces: a new paradigm for thin-shell finite-element analysis. *Int. J. Numer. Meth. Engineering*, 47, (2000), 2039–2072.
- Cirak, F.; Radovitzky, R.: A Lagrangian-Eulerian shell-fluid coupling algorithm based on level sets. *Computers & Structures*, 83, (2005), 491–498.
- Cuitino, A.; Ortiz, M.: A material-independent method for extending stress update algorithms from small-strain plasticity to finite plasticity with multiplicative kinematics. *Engineering Computations*, 9, (1992), 437–451.
- Davis, S. F.: Simplified second-order Godunov-type methods. *SIAM J. Sci. Stat. Comp.*, 9, (1988), 445–473.
- deBorst, R.: The zero-normal stress condition in plane-stress shell elasto-plasticity. *Comm. Meth. Appl. Numer. Meth.*, 7, (1991), 29–33.
- Deiterding, R.: AMROC - Blockstructured Adaptive Mesh Refinement in Object-oriented C++. Available at <http://amroc.sourceforge.net> (2002).
- Deiterding, R.: An adaptive Cartesian detonation solver for fluid-structure interaction simulation on distributed memory computers. In: A. Deane, ed., *Parallel Computational Fluid Dynamics - Theory and Application, Proc. Parallel CFD 2005 Conference*, pages 333–340, Elsevier (2006).
- Deiterding, R.; Cirak, F.; Mauch, S. P.; Meiron, D. I.: A virtual test facility for simulating detonation-induced fracture of thin flexible shells. In: V. N. Alexandrov; G. D. van Albada; P. M. Slood; J. Dongarra, eds., *Proc. 6th Int. Conf. Computational Science, Reading, UK, May 28-31, 2006*, vol. 3992 of *Lecture Notes in Computer Science*, pages 122–130, Springer (2006a).

- Deiterding, R.; Radovitzki, R.; Mauch, S.; Cirak, F.; Hill, D. J.; Pantano, C.; Cummings, J. C.; Meiron, D. I.: Virtual Test Facility: A virtual shock physics facility for simulating the dynamic response of materials. Available at <http://www.cacr.caltech.edu/asc> (2006b).
- Deiterding, R.; Radovitzky, R.; Mauch, S. P.; Noels, L.; Cummings, J. C.; Meiron, D. I.: A virtual test facility for the efficient simulation of solid materials under high energy shock-wave loading. *Engineering with Computers*, 22, 3-4, (2006c), 325–347.
- Deshpande, V. S.; Heaver, A.; Fleck, N. A.: An underwater shock simulator. *Royal Society of London Proceedings Series A*, 462, 2067, (2006), 1021–1041.
- Fedkiw, R. P.: Coupling an Eulerian fluid calculation to a Lagrangian solid calculation with the ghost fluid method. *J. Comput. Phys.*, 175, (2002), 200–224.
- Fedkiw, R. P.; Aslam, T.; Merriman, B.; Osher, S.: A non-oscillatory Eulerian approach to interfaces in multimaterial flows (the ghost fluid method). *J. Comput. Phys.*, 152, (1999), 457–492.
- Giordano, J.; Jourdan, G.; Burtschell, Y.; Medale, M.; Zeitoun, D. E.; Houas, L.: Shock wave impacts on deforming panel, an application of fluid-structure interaction. *Shock Waves*, 14, 1-2, (2005), 103–110.
- Jones, N.: *Structural Impact*. Cambridge University Press (1989).
- LeVeque, R. J.: *Finite volume methods for hyperbolic problems*. Cambridge University Press, Cambridge, New York (2002).
- Löhner, R.; Baum, J.; Charman, C.; Pelessone, D.: Fluid-structure interaction simulations using parallel computers. vol. 2565 of *Lecture Notes in Computer Science*, pages 3–23, Springer (2003).
- Mauch, S. P.: *Efficient Algorithms for Solving Static Hamilton-Jacobi Equations*. Ph.D. thesis, California Institute of Technology (2003).
- Mauch, S. P.; Meiron, D. I.; Radovitzky, R.; Samtaney, R.: Coupled Eulerian-Lagrangian simulations using a level set method. In: K. Bathe, ed., *2nd M.I.T. Conference on Computational Fluid and Solid Mechanics*, M.I.T., Cambridge, MA (2003).
- Mittal, R.; Iaccarino, G.: Immersed boundary methods. *Annu. Rev. Fluid Mech.*, 37, (2005), 239–261.
- Ortiz, M.; Pandolfi, A.: Finite-deformation irreversible cohesive elements for three-dimensional crack-propagation analysis. *Int. J. Numer. Meth. Engineering*, 44, (1999), 1267–1282.
- Qui, X.; Deshpande, V. S.; Fleck, N. A.: Dynamic response of a clamped circular sandwich plate subject to shock loading. *Int. J. Numer. Meth. Engineering*, 71, (2004), 637–645.
- Shyue, K.-M.: An efficient shock-capturing algorithm for compressible multicomponent problems. *J. Comput. Phys.*, 142, (1998), 208–242.
- Shyue, K.-M.: A volume-fraction based algorithm for hybrid barotropic and non-barotropic two-fluid flow problems. *Shock Waves*, 15, (2006), 407–423.
- Specht, U.: *Numerische Simulation mechanischer Wellen an Fluid-Festkörper-Mediengrenzen*. No. 398 in VDI Reihe 7, VDU Verlag, Düsseldorf (2000).
- Toro, E. F.: *Riemann solvers and numerical methods for fluid dynamics*. Springer-Verlag, Berlin, Heidelberg, 2nd edn. (1999).
- Toro, E. F.; Spruce, M.; Speares, W.: Restoration of the contact surface in the HLL-Riemann solver. *Shock Waves*, 4, (1994), 25–34.
- Xie, W. F.; Liu, T. G.; Khoo, B. C.: Application of a one-fluid model for large scale homogeneous unsteady cavitation: The modified Schmidt model. *Computers & Fluids*, 35, (2006), 1177–1192.

Address: R. Deiterding (corresponding author), Oak Ridge National Laboratory, P.O. Box 2008, MS-6367, Oak Ridge, TN 37831, USA.
email: deiterdingr@ornl.gov.